RAA 2015 Vol. **15** No. **5**, 673–686 doi: 10.1088/1674–4527/15/5/006
http://www.raa-journal.org *http://www.iop.org/journals/raa*

***R**esearch in*
***A**stronomy and*
***A**strophysics*

High resolution deep imaging of a bright radio quiet QSO at $z \sim 3$ *

Yi-Ping Wang[1], Wei He[1], Toru Yamada[2], Ichi Tanaka[3], Masanori Iye[4] and Tuo Ji[5]

[1] Key Laboratory of Optical Astronomy, National Astronomical Observatories, Chinese Academy of Sciences, Beijing 100012, China; *ypwang@bao.ac.cn*
[2] Tohoku University, Aramaki, Aoba, Sendai 980-8578, Japan
[3] Subaru telescope, National Astronomical Obs. of Japan, 650 North A'ohoku Place, Hilo, Hawaii 96720, USA
[4] National Astronomical Obs. of Japan, 2-21-1 Osawa, Mitaka Tokyo 181-8588, Japan
[5] Polar Research Institute of China, Shanghai 200136, China

Received 2014 June 27; accepted 2014 September 25

Abstract We have obtained deep J and Ks-band images centered on a bright radio quiet QSO UM 402 ($z_{\rm em} = 2.856$) using the IRCS camera and adaptive optics systems that are part of the Subaru Telescope, as well as retrieved WFC3/F140W archive images of this object. A faint galaxy ($m_k = 23.32 \pm 0.05$ in the Vega magnitude system) that lies $\sim 2.4''$ north of the QSO sightline has been clearly resolved in all three deep high resolution datasets, and appears as an irregular galaxy with two close components in the Ks-band images (separation $\sim 0.3''$). Given the small impact parameter ($b = 19.6$ kpc, at $z_{\rm lls} = 2.531$), as well as the red color of $(J - Ks)_{\rm Vega} \sim 1.6$, it might be a candidate galaxy giving rise to the Lyman Limit system absorption at $z_{\rm abs} = 2.531$ seen in the QSO spectrum. After carefully subtracting the point spread function from the QSO images, the host galaxy of this bright radio quiet QSO at $z \sim 3$ was marginally revealed. We placed a lower limit on the host component of $m_k \sim 23.3$ according to our analyses.

Key words: galaxies: active — galaxies: high redshift — quasars: general — instrumentation: adaptive optics

1 INTRODUCTION

Recent cosmological simulations have made significant progress on the understanding of the physical properties of quasar absorption line systems and their implications for the ionizing background. Lyman Limit systems (LLSs), as a member of the quasar absorption line (QAL) family, are defined to be optically thick at the Lyman limit($\lambda < 912$ Å) and have a neutral hydrogen column density of $N_{\rm HI} > 10^{17}{\rm cm}^{-2}$. These objects have attracted much attention in recent years. The numerical simulations by Fumagalli et al. (2011) suggest that cold gas streams of a circumgalactic medium

∗ Supported by the National Natural Science Foundation of China.
† Based on data collected at the Subaru Telescope, which is operated by the National Astronomical Observatory of Japan. We acknowledge the use of HST WFC3 archive data.

mostly appear as LLSs ($N_{\rm HI} > 10^{17}\ {\rm cm}^{-2}$), while gas clumps in the streams give rise to damped Lyman Alpha systems (DLAs) ($N_{\rm HI} > 10^{20.3}\ {\rm cm}^{-2}$) as well. Meanwhile, the simulations show that cold streams are unlikely to produce the large equivalent widths of low-ion metal absorption lines, indicating they may arise from outflows.

Although sophisticated numerical simulations with much higher resolution are available today, the questions on the physical origin of the absorption lines, i.e. whether the absorbing gas primarily traces the cool extended regions of dark matter halos, dwarf satellite galaxies, galactic disks or supernovae-driven outflows, still remain in dispute (Katz et al. 1996; Kohler & Gnedin 2007; Prochaska et al. 2010; Dekel et al. 2009; Fumagalli et al. 2011; Rahmati & Schaye 2014). For example, Erkal (2014) studied LLSs using simulations which had higher spatial and mass resolution than that of Kohler & Gnedin (2007), and concluded that the majority of LLSs reside in low-mass halos, opposite to what Kohler & Gnedin (2007) have found. However, we understand that the treatment of the complicated physical processes in the simulation would cause uncertainties, and observational evidence and good statistics would set constraints to these models in this case.

Deep imaging and spectroscopy of close QSO/galaxy pairs would provide a unique opportunity to study both the gas flows around galaxies and their stellar population, as well as to determine the morphology and orientation of the galactic disks in space. By performing a kinematic comparison of these absorber galaxies and the QSO absorption line systems, we hopefully could effectively investigate matter in the circumgalactic medium, which is being accreted into galaxies or being expelled by galactic wind. Therefore, identifying LLS absorbers using high resolution deep imaging would be a crucial first step in this study, and there has already been a definite improvement nowadays on the detection power of faint intervening galaxies in the QSO sightline both from space and adaptive optics (AO)-assisted ground-based large facilities, especially towards the peak epoch of galaxy formation ($z \sim 3$). Recent work on nearby LLSs demonstrates the importance of extending such a study to the under-investigated high-z universe, which has an abundance of galaxy formation activities (Stocke et al. 2010; Ribaudo et al. 2011).

On the other hand, studies of high-z quasar hosts have also received increasing attention lately, since they open an important avenue for understanding the assembly and evolution of massive galaxies, in particular in relation to the growth of their central black holes. Although deblending the host components of high-z QSOs from the bright central AGNs is non-trivial, previous efforts in this endeavor have made significant progress by utilizing high resolution images from space (*HST*) and AO techniques of large ground-based facilities. A sample of faint or medium-bright QSOs, including radio loud QSOs (RLQs) and radio quiet QSOs (RQQs) at $z \sim 2-3$, have been observed, especially with the NICMOS camera on *HST* (Ridgway et al. 2001; Kukula et al. 2001; Peng et al. 2006). Moreover, ground-based 8 m class telescopes, especially with AO, offer high spatial resolution for a powerful detection of high-z QSO host galaxies (Falomo et al. 2008; Schramm et al. 2008; Wang et al. 2013). However, properties of the hosts from studies of the current sample have been the subject of some debate. Except for the study by Falomo et al. (2008) that resolved a large host galaxy of a medium-bright RLQ at $z \sim 2.9$, we lack evidence about the peak epoch of galaxy formation at $z \sim 3$, especially related to luminous QSOs.

UM 402 is a bright, high redshift RQQ discovered by MacAlpine & Lewis (1978). It is bright enough to permit detailed spectroscopic observations with a resolution ranging from a few to hundreds of ${\rm km\,s^{-1}}$, and clearly shows strong and sharp Lyman α and CIV emission lines, as well as an LLS at $z = 2.531$ ($N_{\rm HI} > 4.6 \times 10^{17}\ {\rm cm}^{-2}$) even with a low-resolution spectrum (Sargent et al. 1989). Previous deep imaging in the optical band of the field for this QSO indicated the detection of several close neighbors ($\theta \sim 4.7'' - 7''$), which were all spectroscopically confirmed at redshift $z < 1$ (Le Brun et al. 1993; Guillemin & Bergeron 1997). Thus, the galaxy counterpart of the LLS seen in the QSO spectrum has still not been identified. It might be much fainter than the previous detection limit of $m_r(3\sigma_{\rm sky}) = 25.2$ or much closer to the QSO sightline.

UM 402 is also one of the high-z QSOs which we selected for a pilot study, using the IRCS camera and AO system that are part of the Subaru telescope. Several issues were carefully considered during the target selection, 1) high-z QSOs near the era of peak QSO activity and cosmic star formation history at $z \sim 2-3$ are especially selected due to their importance in the understanding of the galaxy formation scenario; 2) there should be a bright guide star ($R < 15$) sufficiently close to the QSO sightline ($< 30''$), in order to be observed with the IRCS and AO36 system on the Subaru telescope; 3) the emission lines Hα (6563 Å), Hβ (4861 Å), OII (3727 Å) and OIII (5007 Å) should be avoided when acquiring the observed bands. This is important for studies that estimate the host mass and properties of the host continuum; 4) there exists a suitable calibration star that can be used for point spread function (PSF) calibration, so that the PSF can be subtracted from the QSO images. We will elaborate on this point in Section 2.1.

In this paper, we present the initial results from the deep J and Ks-band images centered on QSO UM 402 ($z_{\rm em} = 2.856$) using the IRCS camera and AO systems on the Subaru Telescope, as well as archived images of this object taken by WFC3/F140W (PI: Dawn Erb, *HST* proposal ID 12471). The cosmological parameters $\Omega = 0.27,\ \Lambda = 0.73$ and $H = 71\,{\rm km\ s^{-1}\ Mpc^{-1}}$ are adopted throughout.

2 OBSERVATIONS

2.1 Selection of an AO Guide Star and PSF Calibration Star

For the Subaru AO36 adaptive optics system, a natural guide star sufficiently close to the sightline of the target is required to act as a reference source to assess the degradation of wavefronts due to atmospheric turbulence. There is a bright star with a magnitude of $R = 13.8$ and an angular distance to UM 402 of $\theta_{\rm GS} \sim 31''$. We selected this bright star as our AO guide star, and expected to obtain an AO corrected PSF better than $0.2''$ if the natural seeing is $< 0.6''$ (Takami et al. 2004).

Usually, the guide star could not be used to directly model the PSF. This is because the PSF is expected to change with the angular distance from the AO guide star, and the actual PSF at the position of the target will be degraded. On the other hand, there will be a problem with saturation for a very bright guide star required for optimal AO correction. In this case, we have to select another PSF calibration star which could be observed in conditions as similar as possible to that of the QSO, i.e. similar magnitude, direction and angular distance from the guide star. We selected a suitable PSF calibration star for UM 402, which has similar brightness and similar guide star distance, but with a guide star angle offset of $\sim 180^\circ$ with respect to the QSO (see Fig. 1 left). We understand that the decrease in Strehl ratio is not isotropic, and the shape of the PSF varies over the whole field of view (FOV). However, Kamann (2008) suggested that it is possibly a good choice to select a calibration star around the corresponding opposite position of the quasar to largely overcome the variability in the PSF. This approach will allow some improvement based on detailed studies of the residuals in AO-corrected images after the subtraction of the central PSF in the FOV. The details of the QSO, the guide star and the PSF calibration star are listed in Table 1. The guide star used for AO correction is the same one used for QSO and the PSF calibration star.

2.2 Observations and Data Reduction

The AO-assisted Ks band deep imaging of UM 402 was made on 2003 September 17-19 (UT), using the IRCS camera on the Subaru 8.2 m telescope at Mauna Kea and the Subaru Cassegrain AO system with a 36 element curvature wavefront sensor, as well as a bimorph-type deformable mirror with the same number of elements (AO36; Takami et al. 2004). The camera uses one 1024×1024 InSb Aladdin III detector and has two imaging modes with different pixel scales. In the observation, we adopted a pixel scale of $0.023''$ (23mas mode), providing an FOV of $23''\times 23''$(IRCS; Kobayashi et al. 2000). In order to remove bad pixels, we adopted nine-point dithering in a 3×3 grid with a

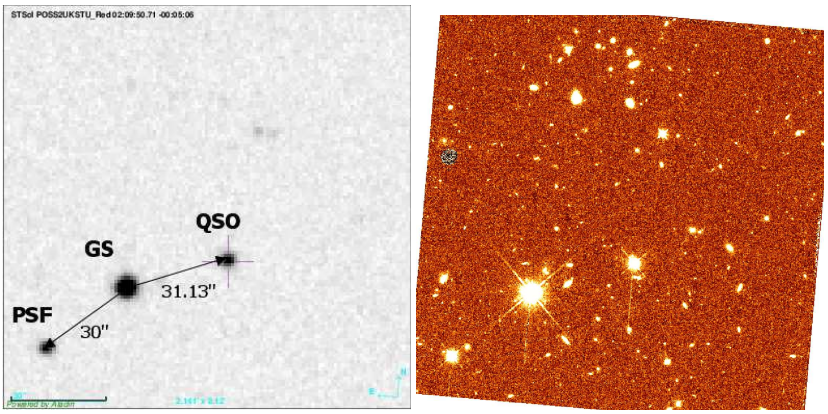

Fig. 1 *Left*: Finding chart for the QSO, guide star (GS) and PSF calibration star from STScI POSS2UKSTU-Red. *Right*: A dither-combined WFC3/F140W image of a region with area $\sim 2' \times 2'$ around QSO UM 402, from one orientation in a single orbit. The pixel scale is $0.13''$. North is up and East is to the left.

Table 1 Observed QSO, PSF Star and the Guide Star

Obj.	Type	RA(J2000)	Dec(J2000)	z	$R_{\rm mag}$	$t_{\rm exp}$(h)[a]	FWHM[b]	Ks[c]	GS(d)[d]
UM 402	RQQ	02 09 50.71	–00 05 06.6	2.855	15.8	3.0	0.13	14.54	31
PSF star		02 09 54.51	–00 05 34.0		16.6	1.0	0.11	15.47	30
Guide star		02 09 52.84	–00 05 15.2		13.8				

Notes: [a] Good exposure times; [b] Image quality as measured by the FWHM for the coadded Ks images of all good exposures in arcseconds; [c] Observed K magnitude of the target for the coadded Ks images; [d] Distance in arcsec from the QSO (PSF star) to the guide star.

dithering step of $5''$, $6.5''$ or $7''$. To reduce the readout noise, the 16-times nondestructive readout was applied during the observation. Dark frames and dome flats were taken at the end of each night. Most of the observing nights were clear and photometric. The median seeing size was $\sim 0.5''$ and the airmass was mostly smaller than 1.4. After optimal functionality of the AO system was achieved, we offset the FOV of the telescope to put the QSO or the PSF calibration star in the center of the FOV.

Similar to the other currently available AO systems, our observations suffered from the small FOV, and we were not able to simultaneously include a suitable PSF calibration star in the QSO exposures to directly evaluate the PSF. In order to monitor and assess the temporal variability of the PSF, we observed the PSF calibration star just before and after the observations of the QSO. More specifically, we observed the QSO itself in an exposure set of 9×80 s, or 9×70 s using the 3×3 dithering pattern, nested between similar dithering observations of the PSF calibration star. Such interleaved observations could provide us with information on the temporal variation of the PSF during the target observations. In addition, such non-simultaneous PSF calibration would provide very similar correction quality for the AO systems to the QSO images, since the variability applies to both the PSF star exposures and the QSO images displaying similar values for the Strehl ratio.

We adopt the "core width r_{20}", which is defined to encircle 20% of the total flux of a point source, as the image quality indicator based on a close relation between r_{20} and the Strehl ratio given by Kuhlbrodt et al. (2005). We measured the r_{20} value of the QSO and the PSF calibration star for each exposure frame of all three observing nights, and only adopted good exposures with $r_{20} < 3.5$ pix (Strehl ratio $S \sim 50\%$ according to the empirical relation of the r_{20} vs. Strehl

ratio). Our further analysis and discussion on properties of the host galaxy mostly rely on these good exposures.

We used the package "IRCS-IMGRED" and the acquired dark frame, flat field, bad pixel mask and sky frame to perform flat field correction and sky subtraction (Minowa 2008). Finally, the dithered frames of the QSO and the PSF calibration star were aligned and averaged respectively, using an outlier rejection algorithm. Values for the full width at half maximum (FWHM) of the AO-corrected and combined QSO image from this run are $\sim 0.13''$ and $\sim 0.11''$ for calibration star images respectively (see Table 1).

In order to constrain the redshift range of the resolved faint galaxy near the QSO sightline, we obtained further deep J-band imaging of the field centered on UM 402 using the IRCS camera and AO188 on the Subaru telescope on 2012 October 5 (UT), in service mode. In this run, we adopted a pixel scale of $0.052''$ (52mas mode), providing an FOV of $54''\times\ 54''$. The weather conditions during the observation were very good and the achieved FWHM in the J-band was $\sim 0.2''$. Total exposure time for the target was two hours. We show the final combined J-band and Ks-band QSO images in Figure 2 (upper right).

To estimate the value of the Strehl ratio in the AO-corrected images, we assume that the PSF can be approximated by a double 2d-gaussian profile as

$$f_{\rm psf} = \frac{f_{\rm core}}{2\pi\sigma^2_{\rm core}} \exp\Big[-\Big(\frac{x^2}{2\sigma^2_{\rm core}} + \frac{y^2}{2\sigma^2_{\rm core}}\Big)\Big] + \frac{f_{\rm halo}}{2\pi\sigma^2_{\rm halo}} \exp\Big[-\Big(\frac{x^2}{2\sigma^2_{\rm halo}} + \frac{y^2}{2\sigma^2_{\rm halo}}\Big)\Big],$$

where $f_{\rm core}$ is the ratio of flux from the diffraction core corrected by the AO system to the total flux (*http://tmt.mtk.nao.ac.jp/ETC_readme.html*); $f_{\rm halo}$ is the flux ratio of the uncorrected (seeing limited) halo to the total flux, and $f_{\rm halo} + f_{\rm core} = 1$; $\sigma_{\rm core}$ and $\sigma_{\rm halo}$ are the spatial broadening of an AO-corrected core and an uncorrected halo respectively. We fitted the AO-corrected and combined J and Ks-band QSO or calibration star images using a Markov Chain Monte Carlo method. The Strehl ratio is estimated as: $Strehl = f_{\rm core} + f_{\rm halo} \times (\frac{\sigma_{\rm core}}{\sigma_{\rm halo}})^2$, which gives a value of $\sim 39\%$ for the J-band image and $\sim 41\%$ for the Ks-band image.

The standard stars FS 110, P533-D and P338-C were observed for photometric calibration, which were selected from Hawarden et al. (2001).

2.3 PSF Construction and Subtraction

Our goal with the high resolution AO images is to detect faint galaxies along the QSO sightline, as well as the faint extended host galaxy hidden in the glare of light from the central bright QSO. Therefore, it is mandatory to properly estimate the AO PSF and subtract the light contribution from the bright central point source in the QSO images, in order to unveil the faint objects underneath, and to reduce their bad effects in photometric measurements.

For the deep Ks-band images, the PSF calibration star was observed as we described in Section 2.2. Thus, we can create a PSF using interleaved exposures of the PSF calibration star between QSO observations in two ways as follows:

(1) Firstly, we constructed a sigma-clipping averaged PSF from the series of star images that is used for PSF calibration. To detect the host galaxy, we subtracted the PSF from the QSO image using a very conservative and simple method, which is the same as other studies on high-z QSO host galaxies. We scaled the PSF flux to the QSO central peak intensity and aligned them. Such a method implies an oversubtraction of the nuclear component from the inner region, and provides a model independent host detection and a lower limit on the host flux (Sánchez et al. 2004). After PSF subtraction, the residual image of this bright QSO in the Ks-band is shown in Figure 3 (upper right). The contour plots of the QSO images after PSF subtraction for each observing night during Sept. 17 – Sept. 19, as well as the coadded residual images from all three nights, are shown in Figure 4 (left).

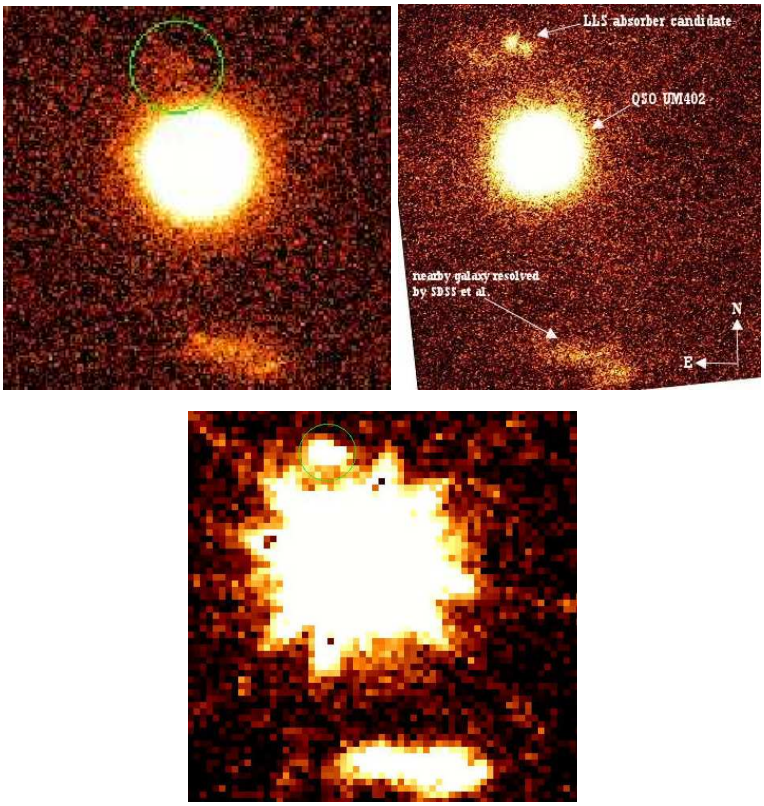

Fig. 2 *Upper left*: A combined image of a region with area $\sim 5'' \times 5''$ around QSO UM 402 (central bright source) in the J-band. The LLS absorber candidate is $\sim 2.4''$ north of the QSO sightline (marked by a circle in the figure). The pixel scale of the J-band image is $0.052''$ and the AO-corrected FWHM $\sim 0.2''$. *Upper right*: A combined Ks-band image of a similar region centered on the QSO like that of the J-band image shown in the left. The LLS absorber candidate is indicated in the figure, and appears as a merging system with two close components having a separation of $\sim 0.3''$. The galaxy south of the QSO sightline has been detected by SDSS and other optical deep imaging projects as a nearby irregular galaxy at $z \sim 0.36$ (Le Brun et al. 1993; Guillemin & Bergeron 1997). The pixel scale of the Ks image is $0.023''$ and the AO-corrected FWHM is $\sim 0.13''$. *Bottom*: A combined WFC3/F140W image of UM 402 (with a pixel scale of $0.13''$), after aligning and de-rotating the two dithered frames from the second orientation. The LLS candidate galaxy is indicated in the figure by a circle. North is up and East is to the left.

(2) Secondly, we applied a principal component analysis (PCA) based on the Karhunen-Loève (KL) transform to construct a PSF from the series of interleaving exposures of the calibration star (Karhunen 1947; Loeve 2006). This algorithm is adopted to quantify the modes in which the PSF varies with time by a basis function that characterizes the temporal variations of the calibration star as well as the QSO images (Chun et al. 2006; Soummer et al. 2012). A $\sim 2.5'' \times 2.5''$ region centered on each reduced frame of the calibration star image was selected as a search area, which is considered to be free from any other astronomical signal. We computed the basis function by calculating the KL transform of the set of calibration PSFs over the ensemble of searching areas. The first 20 modes with the largest eigenvalues of the basis function were selected to construct the best estimation of the actual PSF of the QSO image from the projection of the QSO image

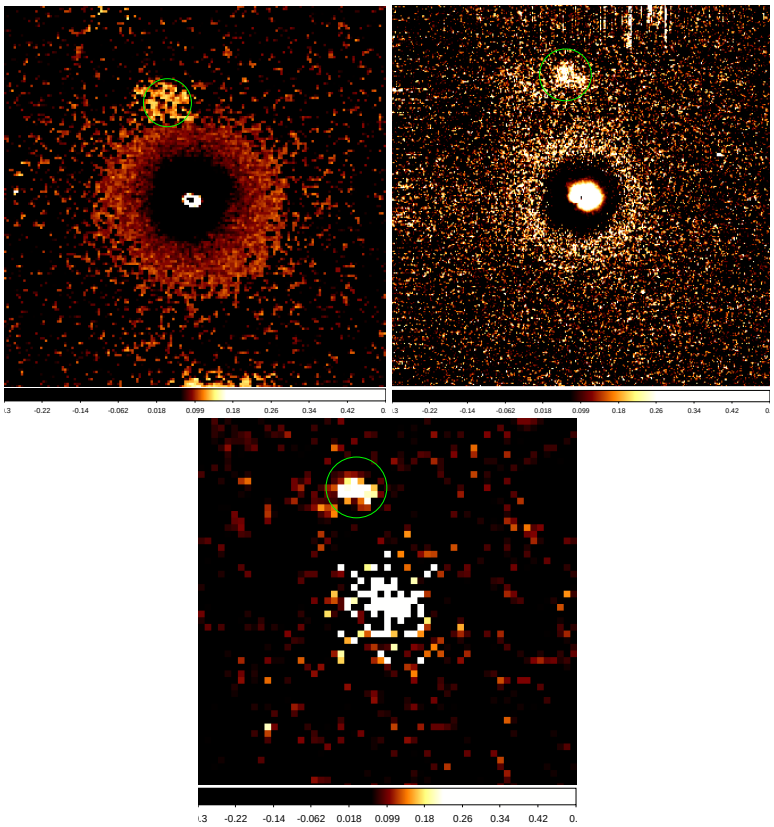

Fig. 3 *Upper left*: A PSF subtracted and coadded J-band image ($0.052''/\mathrm{pix}$) around QSO UM 402. The construction of the PSF model was described in the last paragraph of Section 2.3. *Upper right*: A PSF subtracted and coadded Ks-band image of a similar region centered on the QSO as that of the J-band image shown in the left ($0.023''/\mathrm{pix}$). We constructed an averaged PSF from a series of PSF star images as described in Section 2.3 (the first approach). *Bottom*: A PSF subtracted and coadded WFC3/F140W image of UM 402 ($0.13''/\mathrm{pix}$), after aligning and de-rotating the images after PSF subtraction. The PSF was constructed in a classical way by median combining the aligned frames of other orientations (Rajan et al. 2011). The LLS candidate galaxy is indicated in the figure by a circle. The FOV of the image is $\sim 7.5'' \times 7.5''$.

on the KL basis. We understand that the light from the QSO host galaxy or absorbing galaxies might be mistakenly interpreted as components of the PSF, and thus be oversubtracted from the QSO image. Detailed simulation and discussion of this point will be presented in our next paper (He et al. in preparation). In this work, we simply scale the QSO and the PSF model to make their peak fluxes equal. In this way, it is consistent with the analysis using the first approach, as well as previous studies on high-z QSO host galaxies. The results of this analysis are shown in Figure 4 (right). We notice that the residuals of the PSF subtracted images are mostly similar in terms of morphological structure for the two different approaches to PSF reconstruction, as well as among three consecutive observing nights, although slightly shrunk in the case of PCA. We thus believe that the host galaxy of this bright RQQ towards the peak epoch of galaxy formation at $z \sim 3$ has been marginally resolved.

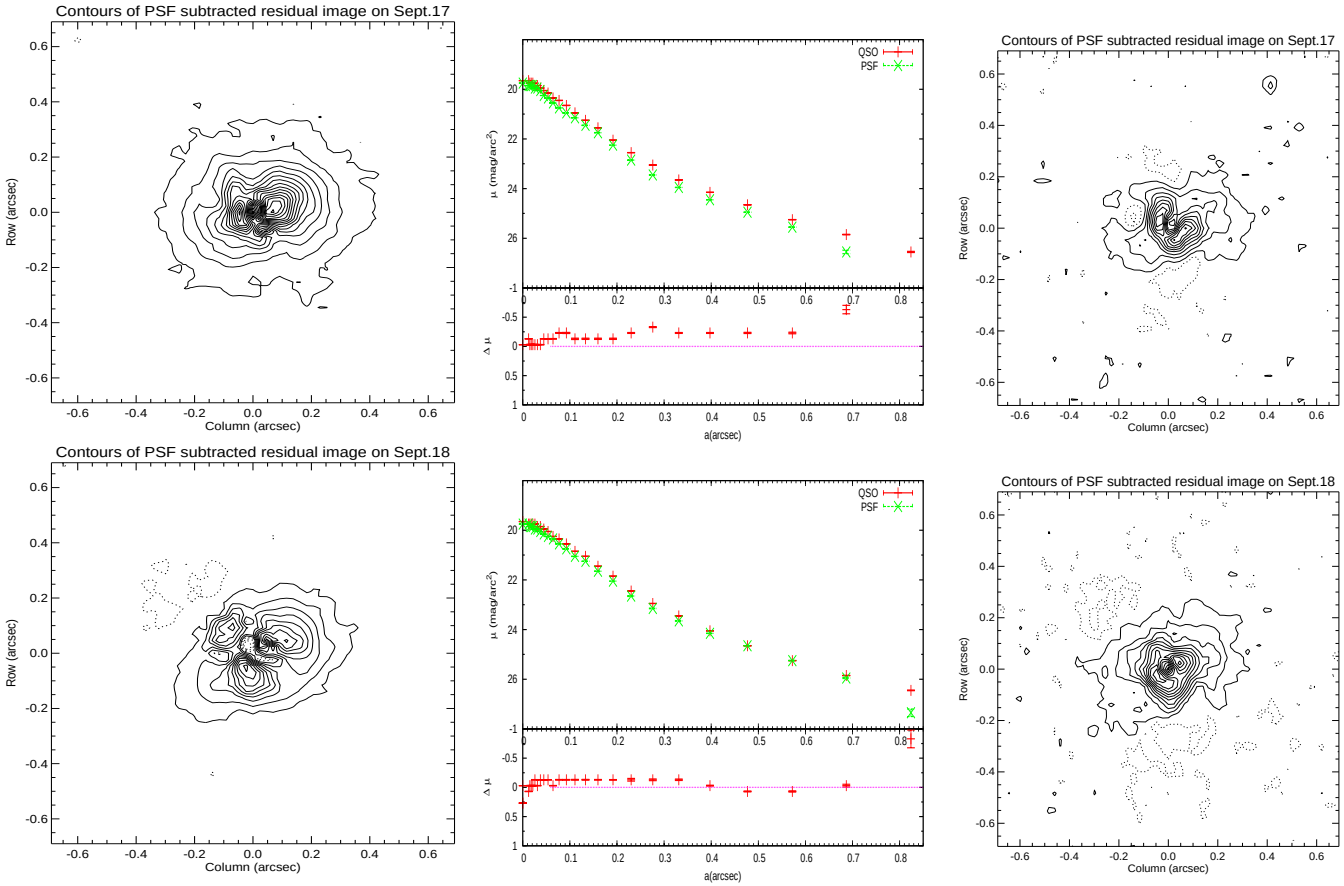

Fig. 4 *Left*: From top to bottom, we show plots of the extended emission of the quasar host revealed after subtracting a PSF from the combined Ks-band images taken on Sept. 17 –19 respectively, and those of all three nights. The PSF was constructed by averaging the PSF star images using an outlier rejection algorithm. *Middle*: The observed radial surface brightness profiles of the QSO (*red pluses*) and the PSF star (*green crosses*) are shown from top to bottom, for the coadded good images of each observing night from Sept. 17 to Sept. 19, as well as those of all three observing nights. *Right*: From top to bottom, we show plots of the extended emission from the good QSO images after PSF subtraction using approach 2) in Section 2.3 for each observing night from Sept. 17 - Sept. 19, as well as those of all three nights. The PSF was constructed from the series of PSF star images using PCA. The contour levels are from pixel values of –0.5 to 3.5 in counts, with an interval of 0.2. We plot the negative contours in dashed lines.

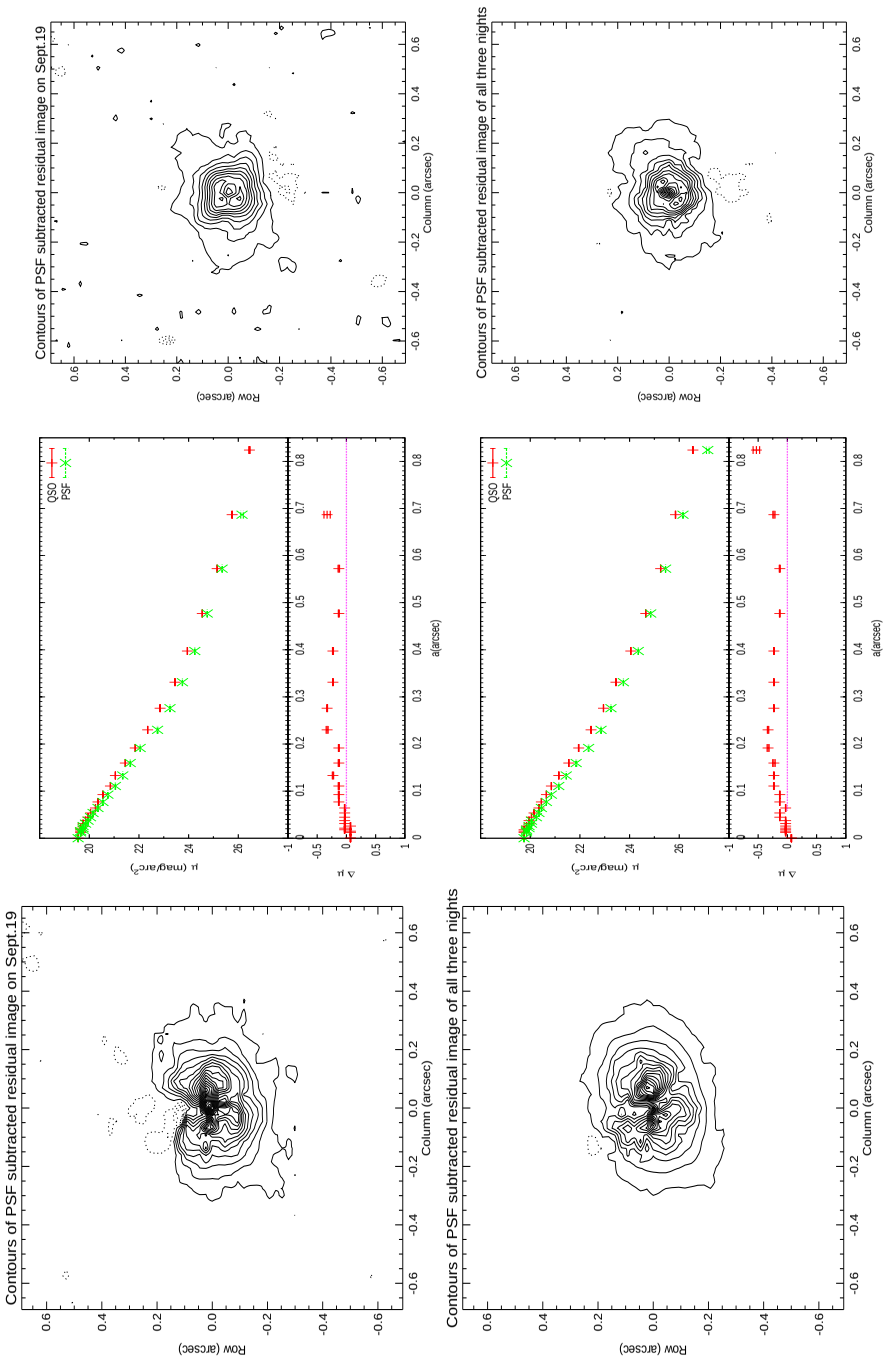

Fig. 4 — *Continued.*

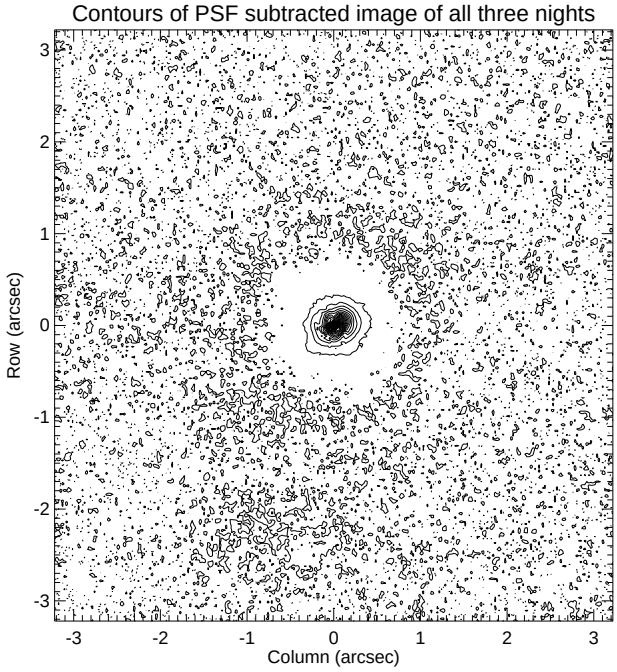

Fig. 5 The contour plot of a region with area $\sim 6'' \times 6''$ centered on QSO UM 402 in the Ks-band, after subtracting a PSF from the co-added images of all three observing nights. The PSF was constructed by coadding the series of nested exposures of the PSF star using an outlier rejection algorithm (the first approach described in Sect. 2.3). The extended emissions of the quasar host are marginally revealed, and the LLS candidate galaxy is visible at the bottom of the plot ($\sim 2.4''$ below the extended emission from the quasar host). The orientation, as well as the contour levels for the plot, is the same as those of Fig. 4. South is up, and East is to the left.

In the interest of only obtaining the $J - Ks$ color of the resolved objects along the QSO sightline, the PSF calibration star was not observed exclusively for the deep J-band imaging using IRCS+AO188, during the service run on 2012 October 5 (UT). Given that IRCS J-band imaging is looking at the wavelength blueward of the 4000 Å Balmer break, we assume that the extended emission from the host galaxy of this QSO is negligible within 2h exposures. In this case, a PSF could be constructed from the series of QSO images after carefully masking out the resolved faint galaxies in the QSO field, using PCA. We finally subtracted the model PSF from the coadded QSO image in a similar way as the one we used for the Ks-band images. The PSF subtracted QSO image in the J-band is shown in Figure 3 (upper left).

2.4 Archived WFC3/F140W Images

WFC3/F140W imaging of this QSO field with the *HST* is available from the MAST archive (PI: Dawn Erb, *HST* proposal ID 12471). The IR wide F140W filter (1.2–1.6 μm) covers the gap between the J and H bands which is inaccessible from the ground. The pixel scale of WFC3 images is $0.13''$/pixel. We retrieved four calibrated, flat-fielded exposures from the archive (two orientations for a single orbit and two dithers for each orientation), where the exposure time is 202.934 seconds for each exposure. Thus, the total exposure time is 811.736 seconds for the WFC/F140W images.

We reduced the WFC3/F140W images using two methods: 1) directly combining the four frames after de-rotating the two dithered frames from the second orientation by 30 degrees and aligning all the four frames (see Fig. 2 bottom); 2) applying PSF subtraction to the QSO images in the classical method presented by Rajan et al. (2011). Specifically, we generated one QSO image by combining the two aligned dithers from each orientation. A PSF image was constructed by median combining the aligned frames of other orientations, and subtracting from the QSO image. The PSF subtracted QSO images were combined into a final image after de-rotating the second orientation by 30 degrees. We show the processed coadded images in Figure 3 (bottom).

3 ANALYSIS

3.1 Galaxies Near the QSO Sightline and the Luminosity

The high resolution images in the J and Ks bands, as well as the WFC3/F140W filter, have two clearly resolved galaxies within a $\sim 5'' \times 5''$ field around UM 402 (see Fig. 2). They are a fuzzy galaxy about $4.7''$ south of the QSO, and a close object $\sim 2.4''$ north of the QSO sightline. In the deep Ks-band images (Fig. 2 upper right), the faint object which lies $\sim 2.4''$ north of the QSO sightline appears as a double system with a separation between the two components of $\sim 0.3''$. Meanwhile, there seems to be a faint tidal-tail like feature towards the southeast of the left component of this double system, suggesting a possible merging system for this object. The fuzzy galaxy south of the QSO sightline has been detected by the Sloan Digital Sky Survey (SDSS) and other optical deep imaging projects as a nearby irregular galaxy at $z \sim 0.36$ (Le Brun et al. 1993; Guillemin & Bergeron 1997).

Using the program SExtractor, we measured the photometry of this faint object in the coadded and PSF subtracted images of all three datasets shown in Figure 3, with a detection threshold of 2.5σ over the sky level for the Ks-band image, a detection threshold of 2σ for the WFC3/F140W image, as well as a 1.5σ detection threshold for the deep J-band imaging. The photometric results of this faint galaxy measured with a small diameter aperture ($0.6''$) and a large diameter aperture ($1.2''$) are presented in Table 2. However, we noticed that the accuracy of PSF subtraction would cause systematic errors in the photometry of the faint objects along the QSO sightline.

Table 2 Photometric Results of the LLS Absorber Candidate

aper. diameter	J app. mag.	J abs. mag.	F140W app. mag.	F140W abs. mag.	Ks app. mag.	Ks abs. mag.
$0.6''$	26.40 ± 0.14	–20.21	24.01 ± 0.37	–22.60	24.25 ± 0.07	–22.00
$1.2''$	25.43 ± 0.10	–21.18	23.65 ± 0.32	–22.96	23.52 ± 0.05	–22.63

For a more reliable photometric measurement without contamination from a neighboring QSO in a nearby field, we also applied the 2-D decomposition algorithm GALFIT to the coadded Ks-band image, where the QSO (Moffat profile), and any other nearby galaxies (Sérsic profiles) in the field were fitted simultaneously to deblend the components, in order to reduce the contaminating flux from the wing in the PSF of the QSO (Peng et al. 2002). The best fitting gives an apparent magnitude of $m_k = 23.32 \pm 0.05$ for the faint galaxy which lies $\sim 2.4''$ north of the QSO sightline, mostly consistent with the measurements using SExtractor which we discussed above.

To estimate the color of this faint object, we adopted the coadded and PSF subtracted Ks-band image as the detection image and a detection threshold of $\mu = 2.5\sigma$ for the sky background (Bertin & Arnouts 1996). The $J - Ks$ colors were determined by re-running the SExtractor in the double-image mode, in which the faint object detected on the "detection image" (in the Ks-band) was measured with the same aperture as the J-band image, giving a result of $(J - Ks)_{\rm Vega} \sim 1.6$.

According to the impact parameter versus column density relation ($b - \log N_{\rm HI}$) for all confirmed DLA and LLS absorbers given by Moller & Warren (1998), we suspect this close double

system might be a candidate galaxy giving rise to the Lyman Limit absorption at $z_{\rm abs} \sim 2.5$ previously seen in the QSO spectrum ($N_{\rm HI} > 4.6 \times 10^{17}$ cm^{-2}). Considering the apparent K-band magnitude versus stellar mass relation for objects at $2.3 < z < 2.6$ from the MOIRCS Deep Survey (MODS), this galaxy would have a stellar mass of $\sim 3 \times 10^9\, M_\odot$ at the low-mass end of the MODS sample (Tanaka et al. 2011).

Further observations of the spectroscopic redshift as well as kinematics of both components in this faint object are strongly required. If confirmed, it would be important evidence of a merging system at high-z that acts as a Lyman Limit absorber.

3.2 Extended Emission from the Host Galaxy

To detect the host galaxy, we carefully subtracted the PSF from the QSO image using two different approaches which we have discussed in Section 2.3. Since we simply and conservatively scaled the PSF peak flux to match the QSO central peak intensity and aligned them in both approaches, the residuals after PSF subtraction from the QSO images imply there is an oversubtracted nuclear component in the inner region, which is a model independent detection of the host and a lower limit on the host flux (Sánchez et al. 2004).

Contour plots of extended emission from the coadded QSO images after PSF subtraction in the Ks-band using the first approach described in Section 2.3 for each observing night from Sept. 17 - Sept. 19, as well as that of the PSF subtracted coadded residual images of all three nights are given in Figure 4 (left). A lower limit for the host magnitude was estimated to be $m_k = 22.3$, $m_k = 23.2$, $m_k = 22.5$ and $m_k = 22.4$ for the images taken on Sept. 17–19 respectively, as well as those from all three observing nights, by photometry on the PSF subtracted QSO image using the SExtractor program (a diameter aperture of $1.2''$). The systematic errors on the photometry of the host galaxy for different observing nights from Sept.17-19 reach about one magnitude. This indicates that PSF variation on different observing nights significantly affects the host detection and its photometric measurement. On the other hand, a more reliable PSF reconstruction algorithm is required in this case.

In Figure 4 (right), we showed the contour plots of the extended emission from the PSF subtracted coadded QSO images using the second approach introduced in Section 2.3 for each observing night from Sept. 17 - Sept. 19, as well as that of all three nights. Here, a model PSF was constructed using principle component analysis based on the KL transform, and was subtracted from the coadded Ks-band QSO images in a consistent way as that of the first approach discussed in Section 2.3, in order to double-check the results. A lower limit of the host magnitude was estimated to be $m_k = 23.6$, $m_k = 23.3$, $m_k = 23.4$, and $m_k = 23.3$ for the images taken on Sept. 17–19 respectively, as well as that of all three observing nights, by photometry on the PSF subtracted QSO image using the SExtractor package (a diameter aperture of $1.2''$). We noticed that the measured host magnitudes of the three consecutive observing nights are basically consistent, and the systematic errors in the photometric measurement of the host galaxy using a PSF reconstruction algorithm based on the PCA are reduced by more than half. This is probably because the PSF reconstructed using PCA would account for most of PSF's temporal variation, which might be smeared out in the case of an averagely combined PSF.

We measured the radial profiles of the coadded images of the QSO and the PSF star ($r_{20} < 3.5$ pix) using the STSDAS task ELLIPSE, after masking out the close companions. The radial profiles of the coadded QSO images from each observing night are compared with the PSF based on stellar profiles acquired during QSO exposures of that night, and those of the coadded QSO and PSF exposures of all three nights, as well as their residuals are presented in Figure 4 (middle).

We noticed from Figure 4 that extended emission from the QSO host galaxy at radii $> 0.2''$ is consistently resolved for almost all three nights using three different analyses, indicating there is a marginally resolved host galaxy associated with this bright RQQ towards the peak epoch of QSO

activity. We can accept a rough lower limit on the host magnitude to be ~ 23.3 based on analyses that we have discussed.

Finally, we zoomed out the contour plot on the left bottom of Figure 4 to provide a larger size for the residual image after PSF subtraction with the faint LLS candidate galaxy visible in the FOV. The LLS candidate galaxy is seen at the bottom of the plot, $\sim 2.4''$ below the extended emission of the quasar host.

4 SUMMARY

We have presented analyses of deep images in the J and Ks bands centered on QSO UM 402 at $z_{\rm em} = 2.856$ using the IRCS camera and the AO systems on the Subaru telescope, as well as the WFC3/F140W archived images of this object.

A faint galaxy ($\sim 2.4''$ north of the QSO sightline) has been clearly resolved by all three high resolution datasets. Especially in the deep Ks-imaging, it appears to be a double system with a separation of the two components $\sim 0.3''$; the faint tidal-tail like feature from the left component of the double system indicates that it is probably a merging system. According to the empirical relation of the impact parameter versus the neutral hydrogen column density of all confirmed DLA and LLS absorbers given by Moller & Warren (1998), as well as its red color $(J - Ks)_{\rm Vega} \sim 1.6$, we suspect that this faint object might be a candidate galaxy giving rise to Lyman Limit absorption at $z_{\rm abs} = 2.531$ previously seen in the QSO spectrum. If the redshift and the kinematics of both components in the double system are spectroscopically confirmed in the future, it would be important evidence of a merging system at high-z that acts as a Lyman Limit absorber.

After carefully subtracting the PSF using two different approaches to PSF reconstruction, we are able to marginally see extended emission from the quasar host galaxy. Since we simply and conservatively scaled the PSF peak flux to match the QSO central peak intensity and aligned them in both approaches, we would obtain oversubtracted extended emission from the quasar host, and can only place a lower limit on the host flux.

Although the residual images after PSF subtraction are mostly similar in terms of morphological structure for the two adopted approaches to PSF construction, as well as among three consecutive observing nights, we noticed that different PSF subtraction algorithms would have large systematic errors on the photometry of the extended host emission. The systematic errors in the photometry of the extended host galaxy during three consecutive observing nights from Sept. 17–19, using the first approach of Section 2.3, reach about one magnitude, where the PSF was constructed by averaging the coadded interleaving exposures of the PSF star. On the other hand, a more reliable PSF reconstruction algorithm, such as PCA (the second approach described in Sect. 2.3), presented a relatively consistent photometric measurement for the host galaxy for the three consecutive observing nights, and possibly places a lower limit of $m_k = 23.3$ for the host galaxy (see the detailed discussion in Sect. 3.2). Further analyses and simulations on how to properly estimate properties of the host are being developed and will be presented in our next work (He et al. in preparation).

Acknowledgements This project/publication was made possible through the support of a grant from the John Templeton Foundation and National Astronomical Observatories, Chinese Academy of Sciences. The opinions expressed in this publication are those of the author(s) and do not necessarily reflect the views of the John Templeton Foundation or National Astronomical Observatories, Chinese Academy of Sciences. The funds from the John Templeton Foundation were awarded in a grant to The University of Chicago, which also managed the program in conjunction with National Astronomical Observatories, Chinese Academy of Sciences. YPW would like to thank Dr. Chien Peng for support on the GALFIT fitting process. YPW acknowledges the Subaru team and Dr. Yosuke Minowa for the hospitality, the National Natural Science Foundation of China (Grant Nos. 10173025, 10673013, 10778709 and 11073031) and the National Basic Research Program of China (973 Program, TG 2000077602). We would like to thank our referee Dr. Michael Strauss for

helpful comments. Some/all of the data presented in this paper were obtained from the Mikulski Archive for Space Telescopes (MAST). STScI is operated by the Association of Universities for Research in Astronomy, Inc., under NASA contract NAS5-26555. Support for MAST for non-HST data is provided by the NASA Office of Space Science via grant NNX13AC07G and by other grants and contracts.

References

Bertin, E., & Arnouts, S. 1996, A&AS, 117, 393
Chun, M. R., Gharanfoli, S., Kulkarni, V. P., & Takamiya, M. 2006, AJ, 131, 686
Dekel, A., Birnboim, Y., Engel, G., et al. 2009, Nature, 457, 451
Erkal, D. 2014, arXiv:1401.6705
Falomo, R., Treves, A., Kotilainen, J. K., Scarpa, R., & Uslenghi, M. 2008, ApJ, 673, 694
Fumagalli, M., Prochaska, J. X., Kasen, D., et al. 2011, MNRAS, 418, 1796
Guillemin, P., & Bergeron, J. 1997, A&A, 328, 499
Hawarden, T. G., Leggett, S. K., Letawsky, M. B., Ballantyne, D. R., & Casali, M. M. 2001, MNRAS, 325, 563
Kamann, N. 2008, Observing Quasars with Adaptive Optics, PhD thesis, Diplomarbeit of Universitat Potsdam
Karhunen, K. 1947, Über lineare Methoden in der Wahrscheinlichkeitsrechnung, Ann. Acad. Science. Fenn, Ser. A.I., 37, 1
Katz, N., Weinberg, D. H., Hernquist, L., & Miralda-Escude, J. 1996, ApJ, 457, L57
Kobayashi, N., Tokunaga, A. T., Terada, H., et al. 2000, in Society of Photo-Optical Instrumentation Engineers (SPIE) Conference Series, 4008, Optical and IR Telescope Instrumentation and Detectors, eds. M. Iye, & A. F. Moorwood, 1056
Kohler, K., & Gnedin, N. Y. 2007, ApJ, 655, 685
Kuhlbrodt, B., Örndahl, E., Wisotzki, L., & Jahnke, K. 2005, A&A, 439, 497
Kukula, M. J., Dunlop, J. S., McLure, R. J., et al. 2001, MNRAS, 326, 1533
Le Brun, V., Bergeron, J., Boisse, P., & Christian, C. 1993, A&A, 279, 33
Loeve, M. 2006, in Processes Stochastigues et Mouvement Brownien, ed. P. Levy (Paris: Hermann)
MacAlpine, G. M., & Lewis, D. W. 1978, ApJS, 36, 587
Minowa, Y. 2008, Subaru Data Reduction Cook Book: Imaging Observation with IRCS, *http://www.naoj.org/Observing/DataReduction/index.html*
Moller, P., & Warren, S. J. 1998, MNRAS, 299, 661
Peng, C. Y., Ho, L. C., Impey, C. D., & Rix, H.-W. 2002, AJ, 124, 266
Peng, C. Y., Impey, C. D., Rix, H.-W., et al. 2006, ApJ, 649, 616
Prochaska, J. X., O'Meara, J. M., & Worseck, G. 2010, ApJ, 718, 392
Rahmati, A., & Schaye, J. 2014, MNRAS, 438, 529
Rajan, A., Soummer, R., Hagan, J., Gilliland, R., & Pueyo, L. 2011, High Contrast Imaging using WFC3/IR, Space Telescope WFC Instrument Science Report
Ribaudo, J., Lehner, N., Howk, J. C., et al. 2011, ApJ, 743, 207
Ridgway, S. E., Heckman, T. M., Calzetti, D., & Lehnert, M. 2001, ApJ, 550, 122
Sánchez, S. F., Jahnke, K., Wisotzki, L., et al. 2004, ApJ, 614, 586
Sargent, W. L. W., Steidel, C. C., & Boksenberg, A. 1989, ApJS, 69, 703
Schramm, M., Wisotzki, L., & Jahnke, K. 2008, A&A, 478, 311
Soummer, R., Pueyo, L., & Larkin, J. 2012, ApJ, 755, L28
Stocke, J. T., Keeney, B. A., & Danforth, C. W. 2010, PASA, 27, 256
Takami, H., Takato, N., Hayano, Y., et al. 2004, PASJ, 56, 225
Tanaka, I., Breuck, C. D., Kurk, J. D., et al. 2011, PASJ, 63, 415
Wang, Y. P., Yamada, T., Tanaka, I., Iye, M., & Ji, T. 2013, in IAU Symposium, 292, eds. T. Wong, & J. Ott, 195